Assessing barrier properties using impedance spectroscopy in a semi-circular, blood-brain barrier on-chip

Fotios Avgidis

BIOS - Lab on a Chip group, MESA+ Institute of Nanotechnology, Technical Medical Centre, and Max Planck Center for Complex Fluid Dynamics, University of Twente, The Netherlands

May 13, 2019

The blood-brain barrier (BBB) is a crucial biological structure that isolates the central nervous system from the rest of the body. Recapitulating BBB functionality on-chip could allow us to evaluate novel neurotherapeutics and understand how different biological components interact to form the BBB. We have developed a microfluidic BBB model that integrates electrodes, allowing for real-time and label-free assessment of the barrier's integrity. Unlike previous efforts, our model reflects the actual size (diameter < 30 μm) and circular shape of a human brain microvessel, and achieves membrane-free separation of the basolateral and apical compartments. Using our BBB, we measured *in vivo*-like TEER values, showed that vitamin C contributes towards a tighter endothelium, and transiently modulated the tightness of the cell layer by locally depleting calcium ions. Finally, we verified the observation that the human cerebral endothelial cells used in this study (cell line hCMEC/D3) form a tight monolayer without the need for endothelial–glial co-culture.

The blood-brain barrier (BBB) is a biological structure that acts as a "gatekeeper" between the peripheral blood circulation and the central nervous system. It tightly controls the flux of solutes from the blood to the brain, only allowing chemicals that are necessary for neuronal functioning. The main structural element of the BBB are micrometer-wide cerebral blood vessels. A network of over 600 km of these capillaries delivers the necessary nutrients to the brain [1]. These capillaries are formed by endothelial cells tightly packed together to form a continuous cylindrical structure. A crucial factor of cerebral capillaries that differentiates them from capillaries in the rest of the body, is the presence of intercellular tight junctions. These tight junctions restrict the paracellular transport of solutes [2]. Disruption of tight junctions is associated with several diseases such as Alzheimer's disease [3], stroke [4], encephalopathy [5], Parkinson's disease [6], and many others. Nevertheless, reversible tight junction disruption can be employed as a gateway for drug delivery to the brain. Hence, high-fidelity *in vitro* models of the BBB could, on the one hand, assist in better understanding the biological origins of diseases that affect the blood-brain barrier and, on the other hand, allow for better screening of novel neurotherapeutics [7].

Although the physiology of the blood-brain barrier has been thoroughly investigated in primary cultures of brain endothelial cells, these traditional cell cultures do not imitate the actual, three-dimensional structure of cerebral blood vessels, and do not allow for label-free assessment of the barrier tightness. The later has been addressed with the advent of the Transwell system. This system consists of two fluidic compartments separated by a porous membrane. Transwell systems allow the insertion of a single electrode in each compartment that can then be used to measure trans-epithelial electrical resistance (TEER), a quantitative measure of the integrity of tight junctions in cell monolayers [8]. Although TEER measurements in Transwells systems are presented very regularly in literature, the TEER values reported show significant variability [9]. This has been attributed to two factors: first, these electrodes are most often manipulated manually, and their location with respect to the porous membrane can affect the resistive readout [10] and second, it is often assumed that the entire cell culture area contributes equally to the measurement, which has been shown to be false [11].

A recent alternative to the Transwell system are microfluidic models of the blood-brain barrier that allow for better emulation of the physiology of the cortical capillary while consuming minimal amounts of reagents. Over the past few years, several such microfluidic "organs-on-chips" have attempted to imitate blood-brain barrier functionality on a chip while integrating electrodes for the electrical assessment of the barrier tightness. Nevertheless, the vast majority of these models, instead of recreating the three-dimensional structure of a cortical capillary, they rely on a non-physiological membrane that separates a basolateral and apical fluidic compartment [7] [12] [13] [14] [15] [16] [17]. Therefore, all these models recreate a two-dimensional endothelium rather than a three-dimensional capillary. Conversely, a few microfluidic

models of the blood-brain barrier do imitate the actual circular shape of a capillary, but they do not exhibit the appropriate physiologically-relevant size and do not allow for electrical assessment of the barrier tightness [18] [19].

Here, we present a novel human blood-brain barrier model that, unlike previously-reported models, reflects the actual size and circular shape of a human brain microvessel and achieves membrane-free separation of the basolateral and apical compartments of the brain capillary, while still allowing for real-time and label-free assessment of the barrier integrity through an array of integrated electrodes. We have employed finite element modelling to optimize the geometry and placement of the integrated electrodes in order to achieve high sensitivity and linearity between measured resistance and TEER.

Unlike many previously-reported models that relied on the insertion of metal wires acting as electrodes above and below the cultured cells on a chip, that suffer from large measurement variability due to variation in the positioning of the metal wire [7] [17] [20], we chose to use electrodes sputtered on a glass substrate. This allows us to minimize the cost of the device by reusing the same electrodes over multiple microfluidic devices while ensuring that the relative position of the electrode with respect to the channel is always the same. To assess the barrier integrity, we employed 4-point impedance spectroscopy that allows us to extract both cell layer resistance and capacitance while being less prone to the influence of electrode polarization impedance compared to 2-point impedance spectroscopy [11].

To achieve a high-fidelity blood-brain barrier model, it is important to couple the effect of astrocytes to the cortical capillary. Astrocyte coculture has shown to upregulate the expression of tight junctions, enzymes, and transporters [21]. Since, *in vivo*, astrocytes do not make direct contact with endothelial cells, but the two cell types are rather separated by the basal lamina, a 20 to 100-nm thick layer of extracellular matrix [22], we hypothesized that growing the cortical capillary in the presence of astrocyte-conditioned medium should have a similar effect. We elucidated this effect by measuring differences in the barrier tightness of cells grown in the presence and absence of astrocyte-conditioned medium and then challenging them with hydrogen peroxide (H_20_2), a common oxidizer that damages tissue via oxidative stress. The latter is to test the observation that astrocyte coculture upregulates antioxidant enzymes in endothelial cells [23].

We subsequently employed our model to study the role of a common antioxidant, vitamin C, in induced oxidative stress, and finally, the possibility to transiently modulate the tightness of the blood-brain barrier in a dose-dependent manner via altering the calcium concentration of the cell medium.

We simultaneously employed immunofluorescent staining of the tight junction protein ZO-1 to correlate changes in impedance with changes in protein localization.

Materials and methods

Microfluidic device design. The blood-brain barrier on-chip consists of an array of microchannels patterned in Polydimethylsiloxane (PDMS), bonded on a glass substrate with embedded electrodes. Each microchannel has a length of 8 mm and a radius of approximately 27 µm, with the total volume of each microchannel being below 10 nanoliters. Each PDMS device consists of two separate parallel channels. Forty-four platinum electrodes are located at the bottom of each microchannel, used to address different micrometer-long regions of the cortical microvessel independently. The effective area of each electrode is 30 × 60 µm. Electrodes are grouped in sets of four, with the distance between each pair being 200 µm. We arrived at this design through finite element simulations with the purpose of maximizing sensitivity and linearity between measured resistance and TEER. All electrodes have accessible connection pads at the edges of the glass substrate. A holder was designed and milled in acrylic and subsequently fitted with spring contacts to allow the electrical interfacing between the assembled chip and an impedance analyzer.

Microfluidic device fabrication. Microscale features were fabricated on a silicon wafer using the AZ 40XT positive photoresist (Microchemicals GmbH, Ulm, Germany). The photoresist was reflown by ramping the temperature of the wafer from 60°C to 140°C (12°C/min) and then baking it at 140°C for 60 seconds to achieve semi-circular channels with a height of approximately 27 µm. The wafer was then coated overnight with Chlorotrimethylsilane (Sigma-Aldrich, St. Louis, MO, USA) to avoid PDMS adhesion. Polydimethylsiloxane (PDMS) prepolymer (Sylgard 184; Dow Corning, Midland, MI, USA) was then mixed thoroughly with curing agent at a 10:1 mass ratio and the mixture was poured over the silicon wafer containing the microscale structures. Then, the PDMS structure was degassed for 30 minutes in a vacuum desiccator and subsequently cured at 80°C for 2 hours. The PDMS slice with the channel imprints was then peeled from the silicon wafer, and two inlets were punched at either end of each channel using a biopsy puncher with a diameter of 0.5 mm. PDMS devices were then rinsed with isopropanol, ethanol, and distilled water and dried using compressed air. To facilitate the bonding of the PDMS devices to the glass slide containing the sputtered electrodes, both surfaces were activated in an oxygen plasma at 50 W for 40 seconds. If a glass slide was reused, residual

PDMS was removed by immersing the slide in acetone overnight. Alignment of the channel and the electrodes was achieved manually under a stereoscopic microscope. To ensure more permanent sealing of the two surfaces, the bonded devices were placed at 80°C for 90 minutes. The complete device design is shown in figure 1.

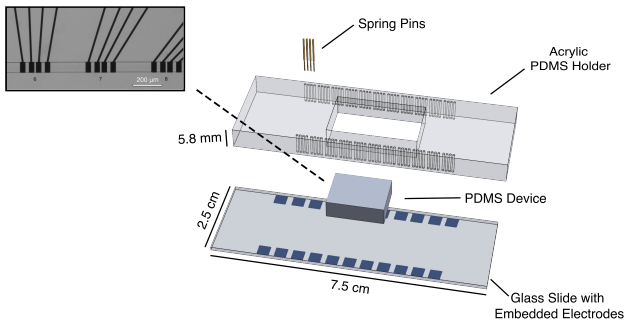

Fig. 1. Exploded view of the device. Inset: phase-contrast image of one of the two channels. Three out of the eleven electrode sets are shown.

Electrical simulations. When using 4-point impedance spectroscopy to measure the impedance of a cell layer, not all sub-volumes of the cell layer contribute equally to the total impedance. Cell volumes closer and between the electrodes contribute more significantly than volumes far from the electrodes. We define a current-carrying pair of electrodes that is used to inject current and a pick-up pair that measures the subsequent voltage drop. The generated field is picked up the strongest by the pick-up pair when it is exactly in line with the field generated by the current-carrying pair [24], supplementary figure 1 illustrates this effect. The sensitivity of a sub-volume is a measure of the contribution of this volume on the total impedance of the call layer, and it is defined as [25] [26]:

$$S = \frac{\boldsymbol{J}_1 \cdot \boldsymbol{J}_2}{I^2} \qquad (1)$$

Where $\boldsymbol{J}_1$ and $\boldsymbol{J}_2$ are the current density fields produced as a result of a current I injected through the current-carrying electrodes and pick-up electrodes, respectively [11]. A larger positive sensitivity value means that the given sub-volume has greater influence on the total impedance. Interestingly, there are also zones of negative sensitivity, where the contribution to the total impedance is underestimated. Using finite element modelling, we performed a series of simulations to determine the optimal electrode configuration to minimize non-linearities in the sensitivity of the system. To calculate the sensitivity, the current I was first injected through the current-carrying electrodes and $\boldsymbol{J}_1$ was extracted, then the same current was injected through the pick-up electrodes and $\boldsymbol{J}_2$was extracted. Since the length of the electrodes is limited by the width of the channel (60 µm) and their height is determined by the fabrication process to be 120 nm, we were free to vary the width of each electrode and the distance between electrodes. We found that the maximum sensitivity for small electrode separation distances scales with the electrode width in the power of 1.6, with the maximum sensitivity always found between the pick-up and current-carrying electrodes (supplementary figure 2). Since the ideal sensitivity is 1, we chose the relatively small electrode width of 30 µm. Next, we varied the separation between all four electrodes in each set, and we found that the sensitivity increases linearly with the separation distance. Interestingly, large separation distances also produced a very large region of negative sensitivity where the minimum sensitivity was approximately 25% of the maximum sensitivity (supplementary figure 3). Lastly, we kept the separation between the two pick-up electrodes at the small distance of 10 µm and varied the separation between the pick-up electrode set and the two current-caring electrodes. We found that the sensitivity scales again linearly with the separation distance but the slope was significantly less steep (supplementary figure 4); therefore, we decided to use a moderate separation distance of 20 µm. The final design is shown in supplementary figure 5A. Next, we simulated the sensitivity assuming a cell layer with a height of 1 µm for two different cell layers: a concave cell layer and a semi-cylindrical cell layer while also varying the TEER of the cell layers (supplementary figure 6). This led to two interesting observations: sensitivity converges to the ideal value of 1 for higher TEER values and for larger channel heights (or smaller cell layer thicknesses). We also observed that between adjacent electrode pairs there is an area of 200 µm were the sensitivity contribution is predominately linear and approaches 1 for the expected TEER values (reported *in vivo* TEER values are in the 1 kΩcm² range [27]). We therefore used the following equation to relate the experimentally measured TEER of that region with the actual TEER of the cell layer:

$$TEER_{measured} = (R - R_{blank})A = \\ = (\rho - \rho_{blank})l_{cell} = \left(\frac{\boldsymbol{E}}{\boldsymbol{J}} - \frac{\boldsymbol{E}_{R\to 0}}{\boldsymbol{J}_{R\to 0}}\right) l_{cell} \qquad (2)$$

Where the resistivity of the cell layer relates to the actual TEER of the cell layer as follows:

$$\rho = \left(\frac{TEER \cdot A}{h}\right) \qquad (3)$$

Using equations 2 and 3, we can also relate the actual TEER of the cell layer with the measured resistance

(figure 2). The two quantities scale linearly, with the only difference between the concave and semi-cylindrical cell layers being a difference in the slope. To simplify the connection topology, we also explored the possibility to measure TEER by utilizing electrodes from two different pairs (supplementary figure 5B), this "interchanged" connection topology reduced the number of necessary connections to the impedance spectroscope from (at least) eight to four (see next section). We performed simulations to determine the sensitivity of this new system (supplementary figure 7). Although the existence of a large negative component is apparent between the pick-up pair and the current-caring electrodes, the region between the two pairs exhibits linear sensitivity behaviour and the scaling between the actual TEER and the measured resistance was very similar to the original topology (figure 2), we therefore decided to use this "interchanged" connection topology for all reported experiments.

Impedance spectroscopy measurements. All impedance measurements were performed using the Zurich Instruments HF2IS Impedance Spectroscope operating in 4-point measurement configuration. Schematics of the connection topologies are shown in supplementary figure 8. Impedance spectra were fitted using a custom Matlab script with the transfer function of an equivalent lumped-element circuit. For the fit we employed least squares curve fitting using the Levenberg–Marquardt algorithm. During measurements, the devices were taped on a heated microscope stage that maintained the temperature at 37°C.

Cell culture. Immortalized human cerebral microvascular endothelial cells (hCMEC/D3 cell line, passages 29 to 36) were cultured in endothelial growth medium (EGM; Cell Applications, Inc., San Diego, CA, USA) in T75 culture flasks, coated with 40 mg/mL human plasma fibronectin (Gibco, Thermo Fisher Scientific, Grand Island, NY, USA) in phosphate buffered saline (PBS; Sigma-Aldrich). Cell cultures were maintained in a humidified water-jacketed incubator (37°C, 5% CO_2) and flasks with > 70% confluency were subcultured, and the remaining cells were seeded in devices. Astrocyte-conditioned medium was obtained by cultivating primary human astrocytes (ScienCell Research Laboratories, Carlsbad, CA, USA) for two days in astrocyte growth medium supplemented with 2% fetal bovine serum, 1% astrocyte growth supplement, and 1% penicillin/streptomycin solution (Gibco). Before cell seeding, the microfluidic channels were coated with 80 mg/mL fibronectin in PBS for at least 4 hours at 37°C. Subsequently, the channels were filled with EGM and stored for an additional 45 minutes at 37°C. Endothelial cells were detached from confluent flasks using 0.05% trypsin-EDTA (Gibco). Cells were resuspended in fresh EGM and diluted to a concentration of $6 \cdot 10^6$ cells/ml which corresponds to approximately 55 cells per microchannel. PBS was pipetted on top of each PDMS device to ensure that the two inlets are at the same hydrostatic pressure and cells were injected through a single inlet using a 0.5 mm syringe needle. This seeding method minimizes the amount of air bubbles in each channel during cell-seeding and ensures that cells are not washed away from the channel due to pressure difference created from a slight mismatch in the fluid volume of the inlets. After 1 hour of static incubation, pipette tips filled with equal amounts of EGM were inserted in both inlets to act as reservoirs. The medium was refreshed daily for the duration of each experiment by inserting new pipette tips filled with fresh medium in the inlets. Depending on the experiment, the endothelial medium was supplemented either with 1 mM ascorbic acid (vitamin C; Sigma-Aldrich) or 50% v/v astrocyte-conditioned medium. In experiments were the tight junctions were transiently modulated, EGM was replaced with either Ethylenebis(oxyethylenenitrilo)tetraacetic acid (EGTA; Sigma-Aldrich) or Adenosine triphosphate (ATP; Sigma-Aldrich) in PBS.

Immunofluorescence. Cells were analysed by immunofluorescence staining for either actin filaments (F-actin) or zonula occludens protein-1 (ZO-1). For F-actin staining, cells were washed with pre-warmed PBS and then fixed for 30 minutes at room temperature with 2.5% v/v Glutaraldehyde (Sigma-Aldrich) in PBS. Following a washing step with PBS, cells were permeated for 15 minutes at room temperature with 0.3% v/v Triton-X (Sigma-Aldrich) in PBS. After washing with PBS, actin filaments were stained with ActinRed and nuclei were stained with NucBlue (2 drops of each dye per 1 mL PBS; ReadyProbes Reagent, Molecular Probes, Life Technologies) for 30 minutes at room temperature. Finally, cells were washed again in PBS. For ZO-1 staining, cells were washed with pre-warmed PBS and then fixed for 20 minutes at room temperature with 2.5% v/v Glutaraldehyde in PBS. Following a washing step with PBS, cells were permeated and blocked for 30 minutes at room temperature with 0.1% v/v Triton-X and 5% bovine serum albumin (BSA; Sigma-Aldrich) in PBS. After washing again with PBS, cells were incubated for 90 minutes at room temperature with 5 µg/mL primary anti-ZO1 antibody (rabbit polyclonal antibody; Thermo Fisher Scientific) and 0.5% BSA in PBS. The cells were then washed with PBS supplemented with 0.1% BSA and incubated for 1 hour at room temperature with 5 µg/mL secondary

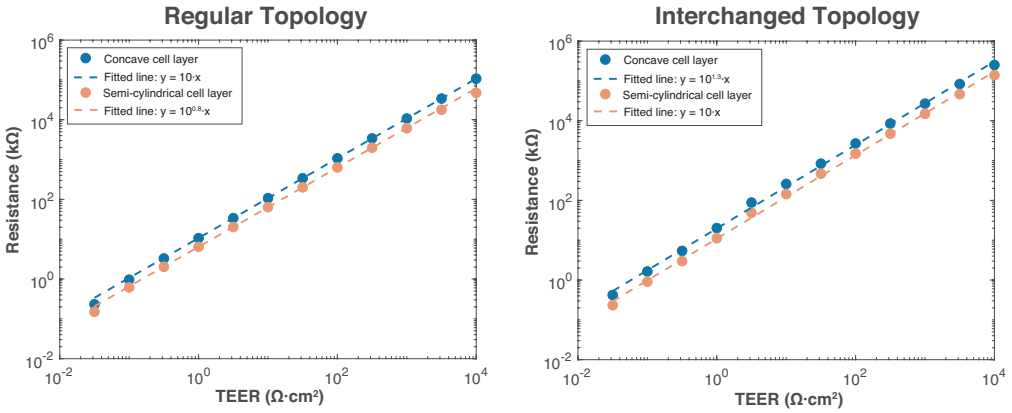

Fig. 2. Simulation results showing the scaling relationship between TEER and measured resistance. For all reported experiments we have used the "interchanged" topology and assumed a semi-cylindrical cell-layer. Therefore, the scaling factor (the slope of the plot) is 10.

antibody conjugated with Alexa Fluor 488 (goat anti-rabbit; Abcam, Cambridge, UK) in PBS.

Finally, the nuclei were stained with NucBlue (1 drop per 1 mL PBS) for 20 minutes at room temperature, and cells were washed a final time in PBS. Images were captured with either a Nikon Instruments A1 confocal laser microscope or with an EVOS M5000 imaging system and analysed with ImageJ.

Tight Junction Quantification. After exposure to ligands, cells in control cultures were analysed using immunofluorescence to correlate the altered localization of the tight junction protein ZO-1 with the change in impedance measured in the microfluidic BBB. Cells in control cultures were grown in glass-bottom wells (GWST-5030; WillCo Wells B.V., Amsterdam, The Netherlands) coated with 80 mg/mL human plasma fibronectin in PBS. For each condition, we performed two to four technical replicates. Cells used for seeding the microfluidic device and the control culture originated from a clonal population. To quantify ZO-1 localization, greyscale images of up to 400 cells for each technical replicate were captured, and the number of localized, cell-to-cell junctions was extracted. All data are expressed as the mean number of localized tight junctions per condition normalized by the number of nuclei ± SEM. Two-sample t-tests for equal means were performed when $N > 3$ to determine statistical significance between different conditions. Differences are considered to be significant when $P < 0.05$. Apoptotic cells (apparent due to the presence of lysosomes) were excluded from the analysis and mitotic cells were counted as a single cell.

Results

Determining the electrical characteristics of the cortical microvessel using impedance spectroscopy. Endothelial cells were seeded in the devices and cultured for up to seven days. The majority of the cells spread and aligned along the long axis of the channel after one day of growth. After static incubation over five days, the resulting microvasculature closely mimicked the size and shape of a human brain microvessel (figure 3). After examining the microchannel using phase-contrast imaging, we selected regions where the microvessel was fully formed and assessed the electrical characteristics of the cell layer by employing the appropriate set of electrodes. A typical impedance spectrum fitted with the transfer function of the equivalent circuit model is shown in figure 4. In this model, a constant-phase element (non-ideal capacitor), CPE, accounts for the impedance associated with the electrode-electrolyte interface [28]. The resistor R_{medium} accounts for the resistance of the medium, while the capacitor C_{cell} and resistor R_{cell} placed in parallel, account for the capacitive and resistive properties of the cell layer, respectively. The Levenberg–Marquardt algorithm used to fit the impedance spectrum requires a set of starting parameters to determine the values of the components of the equivalent circuit model. For R_{medium} we were able to approximate the value using:

$$R_{medium} = \rho \frac{l}{A} \tag{4}$$

Where l is the length of the channel, A the cross-sectional area of the channel, and ρ is the resistivity of the electrolyte, which we measured to be 0.645 Ωm for both PBS and EGM at 37°C. We therefore arrived at a value of approximately 10^5 Ω for R_{medium}. Next, the expression for the impedance of the constant-phase element is:

$$Z_{CPE} = \frac{1}{Y(i2\pi f)^n} \tag{5}$$

Where Y is the capacitance of the constant-phase element and n is an empirical fit parameter reflecting the non-linearity of the element [28]. The values for n lie between 0 (ideal resistor) and 1 (ideal capacitor) while its typical values when used to model double-layer capacitance are 0.8 to 1. Typical values for Y are 20 to 60 µF for every 1 cm² of electrode area [29]. When using these values as starting parameters, the algorithm proved to be robust against a range of initial values for C_{cell} and R_{cell}. Although the selected model fitted well all experimental data, we should note that such fits are phenomenological and should not be over-interpreted, since different combinations of lumped elements might result in an identical fit. Therefore, all experiments on the microfluidic BBB were independently verified using quantitative immunostaining.

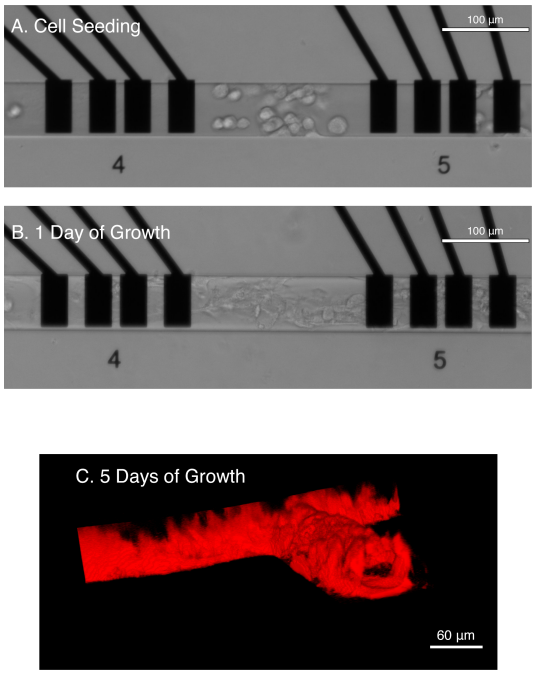

Fig. 3. (A) Phase-contrast image of brain endothelial cells (hCMEC/D3) during seeding. (B) image of the same cells after 24 hours of growth. (C) Confocal image of cell layer after 120 hours of growth (red: F- actin). At the back of the microfluidic channel, the inlet of the device is visible.

Vitamin C contributes towards a tighter endothelium. First, we employed our engineered blood-brain barrier to elucidate the effect of ascorbic acid (vitamin C), a common antioxidant, against oxidative stress. Reactive oxygen species (ROS) that cause oxidative damage are involved in several neurological conditions. We have grown microvessels stemmed from a clonal cell culture in the presence and absence of 1 mM vitamin C and then exposed them to hydrogen peroxide (H_20_2), a ROS that damages tissue via oxidative stress. The recorded impedance data

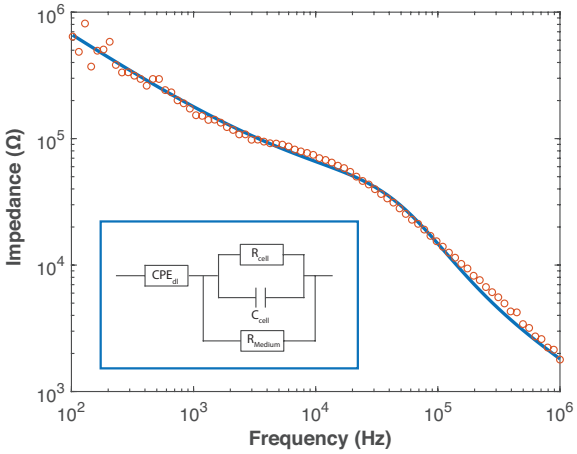

Fig. 4. Typical impedance spectrum (symbols) and fit (solid line). Inset: Equivalent circuit used for the fit.

revealed that a high dose of vitamin C results in a significantly tighter cell monolayer, but the relative change in impedance after H_20_2 incubation is similar in both cases (figure 5). Since capacitance is a proxy for cell membrane surface area [10], and after H_20_2 incubation a number of cells might detach due to weakened tight junctions, we corrected for uneven cell layer coverage by normalizing the cell layer impedance with the cell layer capacitance.

Next, we verified this observation using tight-junction immunostaining on a two-dimensional cell culture. We grew cells in the presence and absence of 1 mM vitamin C and incubated them in varying concentrations of H_20_2. We observed dose-dependent oxidative damage, with higher concentrations of H_20_2 resulting in fewer tight junctions or a punctate localization pattern, although this effect seems to reach a plateau around 50 µM (figure 6). Consistent with the impedance measurements, cells grown in the presence of vitamin C showed higher ZO-1 localization but the relative change in tight junction localization after H_20_2 incubation was similar in both cases. This is consistent with previous reports; Lee *et al.* reported alterations in the ZO-1 localization in bovine brain microvascular endothelial cells after H_20_2 incubation, while they did not report significant changes in ZO-1 protein expression [30]. Moreover, Lin *et al.* reported that Vitamin C prevents BBB disruption in rats after epidural compression of their somatosensory cortex [31].

Collectively, these results indicate that growth in the presence of vitamin C contributes towards a tighter endothelium and hydrogen peroxide treatment results in a leakier blood-brain barrier. However, it is not clear from our data or previous studies whether brain endothelial cells grown in the presence of vitamin C are protected against ROS-induced oxidative damage due to the termination of oxidation reactions by vitamin C.

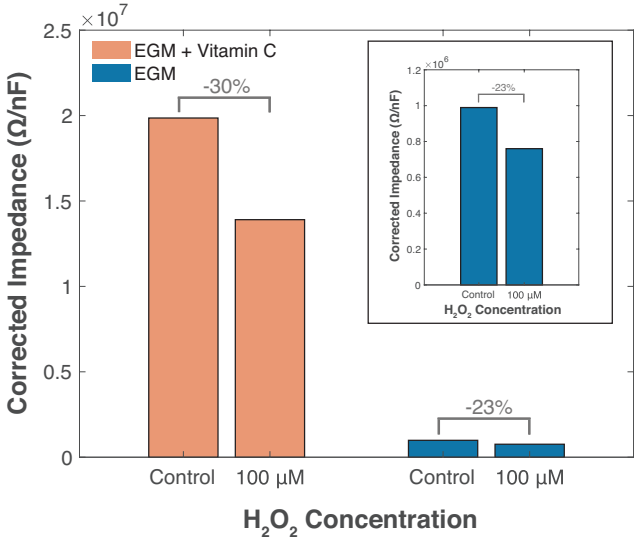

Fig. 5. Impedance measurement in microvasculatures grown in the presence (1 mM) and absence of vitamin C. Inset: enlarged version of the impedance of cells grown in the absence of vitamin C. Cells grown in EGM have an order of magnitude lower corrected impedance compared to cells grown in Vitamin C-supplemented EGM.

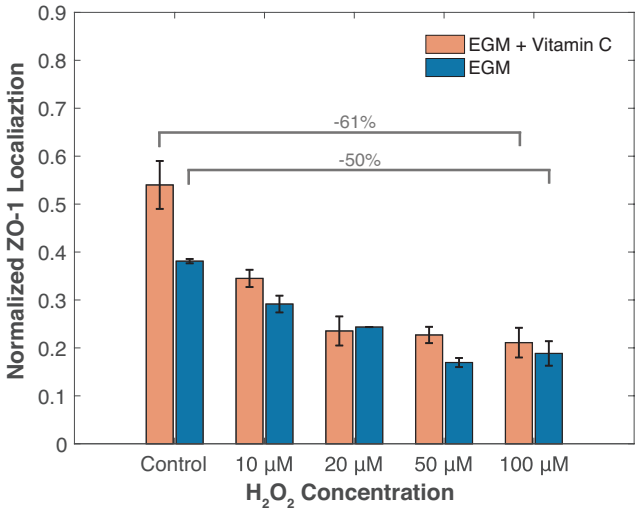

Fig. 6. Immunostaining in a two-dimensional culture reveals that higher H_2O_2 concentrations affect the localization of a larger number of tight junctions. This effect appears to reach a plateau around 50 µM. Error bars represent SEM (2 technical replicates per condition). Individual data points are shown in supplementary figure 9.

Astrocyte-secreted factors do not contribute towards a tighter endothelium. We then explored the effect of astrocytes on the cortical capillary. Astrocytes interact with endothelial cells by wrapping their endfeet protrusions around capillaries. They are known for enhancing tight junction formation, modulating the expression of transporters, and upregulating enzymatic expression [1]. An extracellular matrix layer termed basal lamina separates the endothelial cells and the astrocytic endfeet. Since astrocytes do not make direct contact with endothelial cells and are known to secrete a number of chemical agents, including basic fibroblast growth factor, angiopoietin-1, and glial-derived neurotrophic factor [21], we hypothesized that endothelial growth medium supplemented with astrocyte-derived factors should have a similar effect as co-culturing astrocytes and endothelial cells. Therefore, we obtained astrocyte-conditioned medium (ACM), as described in materials and methods, and supplemented it with the endothelial growth medium (EGM) at a 1:1 volumetric ratio. We subsequently grew microvessels stemmed from a clonal cell culture in the presence of EGM or ACM-supplemented EGM. After incubating the microvessels for 24 hours, we recorded their impedance. Interestingly, the recorded impedance data revealed that the microvessel grown in the presence of ACM had a corrected impedance 72% lower than the impedance of the microvessel grown in EGM (figure 7). This is in agreement with previous experiments using the same immortalized endothelial cell line: Eigenmann *et al.* reported a 50% decrease in TEER after incubating hCMEC/D3 cells in ACM [32]. Likewise, Cucullo *et al.* reported no difference in TEER values when co-culturing hCMEC/D3 cells with human astrocytes compared to hCMEC/D3 monoculture [33]. These results are nevertheless not in agreement with studies using different sources of endothelial cells in their BBB models: Yeon *et al.* incubated human umbilical vein endothelial cells (HUVECs) with ACM for 2 hours and observed reduced permeability to Evans Blue dye, and 4 and 40 kDa FITC-dextrans compared to HUVECs grown in the absence of ACM [34]. Similarly, Siddharthan *et al.* demonstrated that cells from the HBMEC cell line had reduced permeability to FITC-dextran and propidium iodide after ACM incubation for 5 days [35].

Collectively, these results suggest that the hCMEC/D3 cell line imitates the physiology of primary endothelial–glial co-cultures even in the absence of astrocytes. The reduced barrier tightness when hCMEC/D3 cells are incubated in ACM/EGM mixture could be explained by the decreased concentration in growth factors and nutrients this solution has compared to undiluted EGM. This is further supported by the immunostaining experiments we performed (figure 8); when cells are incubated in EGM mixed at a 1:1 volumetric ratio with astrocyte medium, they demonstrate decreased tight junction localization compared to the cells grown in EGM only.

Finally, we exposed the microvessels to hydrogen peroxide, to test the observation that astrocyte co-culture upregulates antioxidant enzymes in endothelial cells [21]. The relative change in normalized impedance was similar in both cases (21% vs 30%) and EGM-grown cells exhibited a smaller relative change (figure 7), which suggests that no upregulation of antioxidant enzymes takes place after

ACM incubation. This is also supported by the immunostaining experiments (figure 8).

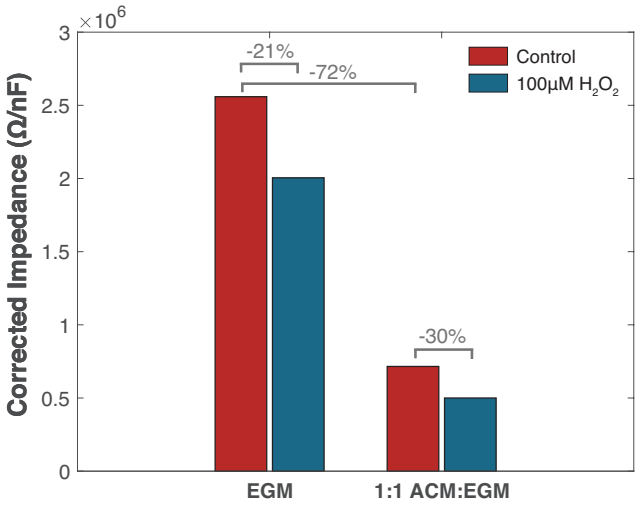

Fig. 7. Impedance measurement in microvasculatures grown in EGM and in 1:1 v/v ACM:EGM mixture. The corrected impedance of the EGM-grown cells is, as expected, similar to that of the EGM-grown cells in figure 5.

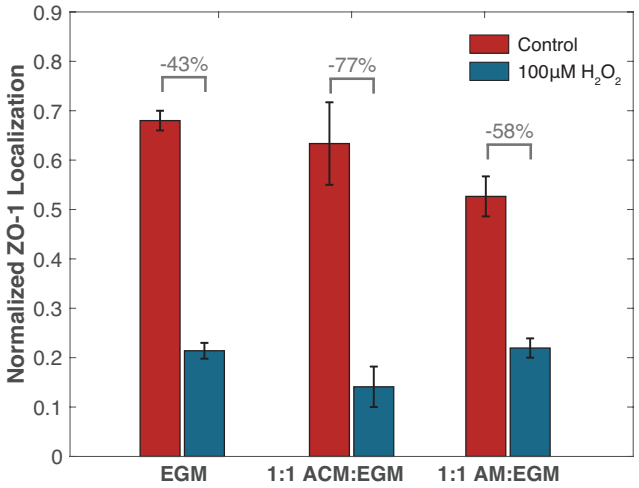

Fig. 8. Immunostaining in a two-dimensional culture shows that supplementation of EGM with ACM or AM results in fewer localized tight junctions. Error bars represent SEM (2 technical replicates per condition). Individual data points are shown in supplementary figure 10.

Varying extracellular and intracellular calcium concentration results in transient modulation of tight junctions. Finally, we explored the possibility of transiently opening the tight junctions. Drug delivery to the brain is greatly hindered by the blood-brain barrier: only molecules with a molecular mass below 400-500 Da and high lipid solubility can cross from the bloodstream to the brain [36]. Nevertheless, since all brain cells are only a few micrometers away from a capillary, once the blood-brain barrier is crossed drugs can quickly diffuse to the whole brain [37]. A way to achieve that is by transiently modulating the tight junctions through local calcium depletion. The assembly of tight and gap junctions requires adherens junctions, and the adherens junctions between endothelial cells contain cadherins, a type of cell adhesion molecule. Extracellular calcium is used to stabilize these cadherins [38]; therefore, depleting calcium from the cell medium should increase the permeability of the cell layer. EGTA, a strong calcium ion chelator, has been tested as a tight junction modulator [39]**.** To verify this, we introduced 5 mM EGTA in a microvessel which resulted in a rapid (within 10 minutes) decrease in the resistance of the cell layer (figure 9). Consistent with previews reports that used the same EGTA concentration [10], microscopic observation of the cell layer revealed that EGTA did not cause any clear cell detachment, making the normalization of the cell layer impedance with the cell layer capacitance unnecessary. We also extracted the resistance of the cell medium from the impedance spectrum before and after the introduction of EGTA and confirmed that the change in the ionic concentration only caused a minimal decrease in the cell medium resistance (figure 9), which is also consistent with previous studies [40]. Although EGTA has high affinity for calcium ions, it also sequesters other metal ions from the cell medium, so a change in medium resistance is expected.

Next, we demonstrated that the decrease in cell layer resistance correlates with a disruption in tight junction-mediated cell-to-cell adhesion. We performed ZO-1 immunostaining in cell layers treated with varying concentrations of EGTA for 90 minutes and observed that the majority of cells detached from each other and a sizeable minority of cells adopted a spherical conformation (figure 10). For higher EGTA concentrations, the immunostaining was predominately cytoplasmic. We quantify these results in figure 11. It is clear that the EGTA-mediated disruption is dose-dependent and our data suggest that calcium is completely depleted at concentrations above 10 mM. Unlike ZO-1 staining following hydrogen peroxide treatment, we observed very few apoptotic cells after EGTA incubation, a corollary of its low cytotoxicity.

Last, we investigated the possibility to modulate extracellular calcium by causing a calcium influx to the cells. Endothelial cells carry a class P2 Purinergic receptor that is activated by ATP and causes a biphasic elevation of cytoplasmic calcium [41]. Calcium is released from intracellular stores, followed by a prolonged influx of calcium across the plasma membrane [38]. This influx of calcium causes a reduction in extracellular calcium which in turn destabilizes tight junctions. To test this effect, we introduced 1 mM ATP in a different microvessel. This, as expected, resulted in a rapid decrease in the resistance of the cell layer (figure 12). This decrease leveled off after 10 minutes of incubation and it was

accompanied by a small increase in the resistance of the cell medium. A possible source of this increase in resistance is an increase in the extracellular potassium content, an ion with high resistivity, caused by the activation of calcium-gated potassium channels.

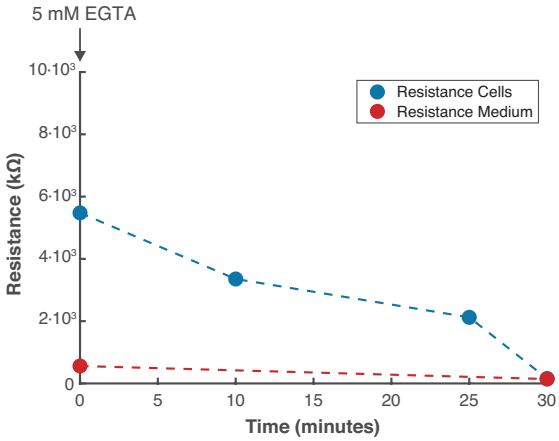

Fig. 9. Time progression of impedance after EGTA introduction. After the data points at t = 0 were recorded, the medium was replaced with 5 mM EGTA added in PBS.

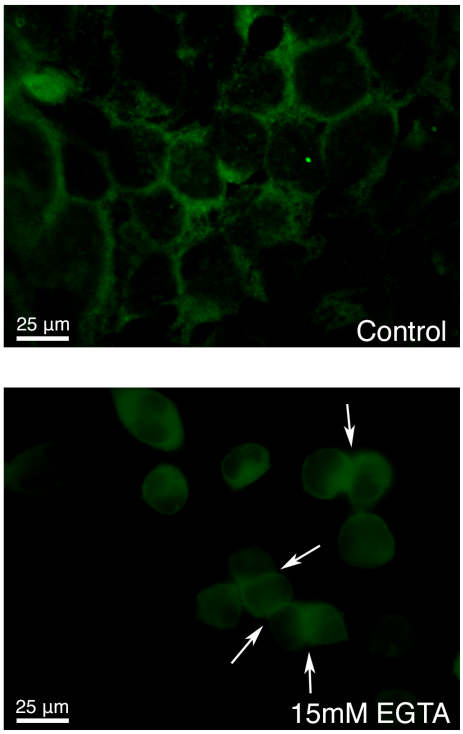

Fig. 10. ZO-1 staining of control culture & cells treated with 15 mM EGTA. Higher intensity staining in the cell borders indicates tight junctions. In the control culture the tight junction staining is continuous, while in the EGTA-treated culture only a few tight junctions are visible (indicated by arrows). The rest of the cells in the culture detached from each other with few cells adopting a spherical shape.

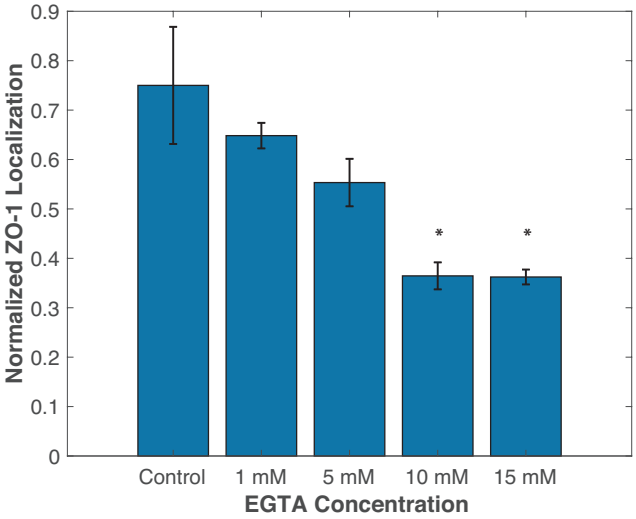

Fig. 11. Immunostaining in a two-dimensional culture reveals the dose-dependent effect of EGTA on tight junctions. Error bars represent SEM (4 technical replicates per condition), asterisks denote significance relative to control. Individual data points are shown in supplementary figure 11.

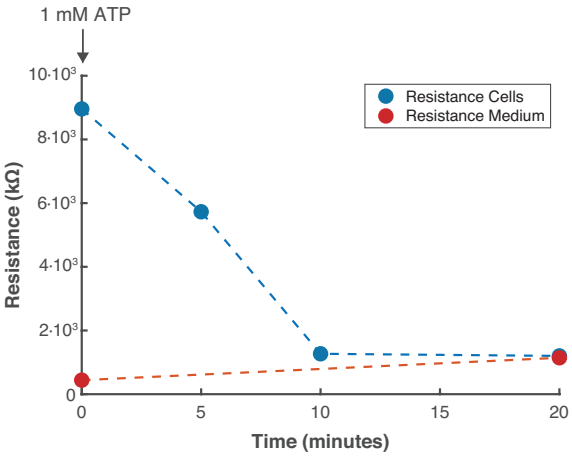

Fig. 12. Time progression of impedance after ATP introduction. After the data points at t = 0 were recorded, the medium was replaced with 1 mM ATP added in PBS.

Discussion

Membrane-free organs-on-chips and their advantages. We have developed a microvascular microfluidic model of the human blood-brain barrier. Our device has a physiologically-relevant shape and size and achieves impedance measurements without the need for a membrane. Membranes are often fabricated from non-physiological materials, introduce an additional electrical resistance to the system, and numerous particles or dyes used for permeability studies can adhere to them. Therefore, membrane-free systems recapitulate *in vivo* physiology more accurately and allow for better permeability assessment. To our knowledge, this is the first blood-

brain barrier microfluidic model that incorporates electrodes for impedance or TEER measurements without the need for a membrane.

Endothelium exhibits *in vivo*-like TEER values. We chose to express all experimental results in either corrected impedance units (Ω/nF) or resistance units (kΩ). Since we designed our system to have a linear relationship between measured resistance and TEER, we can convert the resistance values (expressed in kΩ) to TEER by simply dividing by a factor of 10 (the slope of the plot in the right-hand side of figure 2). We should note that this conversion assumes that the cell layer extends to the whole culture area between electrodes, which in a few cases might not be completely accurate. Since the resistance values we report in this paper are between $5 \cdot 10^3$ and 10^4 kΩ, we arrive at TEER values between 500 and 1000 Ωcm^2. While many previous studies report values between approximately 20 and 300 Ω [42], the values reported here are closer to values expected *in vivo* (TEER values have been estimated to be in the order of 1000 Ωcm^2 *in vivo* [27]). To our knowledge, the only other publication that reports TEER values comparable to *in vivo* values in a microfluidic model is Brown *et al.* [14] (this paper reports TEER values erroneously in Ω/cm^2, van der Helm *et al.* converted their values to the correct TEER units in [42]). While it is tempting to attribute the higher TEER to the physiologically-relevant shape and size of our device, it should be noted that most published results do not consider sensitivity variations and rely on manually-adjusted electrodes that can cause erroneous TEER readouts depending on their positioning [9] [10] [11]. It is therefore likely that these studies report inaccurate TEER values.

General considerations concerning the cell line. All primary and control experiments of the same class were performed with cells of the same passage number to avoid variation due to phenotypic drift, de-differentiation, or senescence. However, expression of the VE-cadherin and β-catenin proteins in the hCMBC/D3 cell line has been shown to remain robust over many passages [43]. Both these proteins are necessary for the establishment of tight junctions. Moreover, this cell line has been shown to form tight monolayers even in the absence of glial cells, such as astrocytes [43]. We verified this observation by growing cells in the presence of ACM. Although having a cell line that forms a tight endothelial monolayer without the need for a co-culture or supplementation with astrocyte-secreted factors is a useful experimental tool, it is clear that this cell line does not fully recapitulate the *in vivo* physiology. It would be interesting to pursue experiments with other cell lines such as the hBMEC cell line that has been shown to have decreased permeability after ACM incubation [35] and overall increased TEER compared to the hCMBC/D3 cell line [32].

Modulating endothelial tightness. We also tested the effect of antioxidants and intracellular and extracellular calcium modulation on the tight junctions. Concerning the effect of antioxidants, it would be interesting to test the effect of other vitamins, such as vitamin E, and compare it to vitamin C. Another possibility would be to test lower concentrations of vitamin C, given that the concentration used here was approximately two orders of magnitude larger than the typical content of endothelial cell growth media. Regarding the modulation of tight junctions, since this effect is reversible, it would be interesting to measure impedance over a more extended period of time, until we observe recovery of tight junctions. In a preliminary experiment using EDTA, a chelating agent with lower calcium specificity compared to EGTA, we observed full recovery of the cell layer resistance within 8 hours (results not shown). Finally, it would be beneficial to expose the cell layer to different concentrations of EGTA and compare the relative changes in resistance. This would allow us to fully verify the results we obtained through immunostaining. Last, we could experiment with different ligands that cause a biphasic elevation of intracellular calcium. Except for ATP, agents such as bradykinin and acetylcholine are known to have a similar effect [38].

First steps towards a system enabling cell co-culture. Finally, a limitation of the device we have developed is that it does not permit the co-culture of different cell types. A potential solution to that would be patterning channels in hydrogel instead of PDMS. This would permit us to culture other cell types such as astrocytes, pericytes, or neurons inside the hydrogel. We have identified a composition of collagen and hyaluronic acid that has sufficient stiffness to support microfluidic channels, developed an ejection mould for the hydrogel, and verified that astrocytes could grow and proliferate inside this gel. We are currently actively pursuing this line of research.

Bibliography

[1] A. D. Wong, M. Ye, A. F. Levy, J. D. Rothstein, D. E. Bergles, and P. C. Searson, "The blood-brain barrier: an engineering perspective," *Front. Neuroeng.*, vol. 6, no. January 2015, 2013.

[2] B. Obermeier, R. Daneman, and R. M. Ransohoff, "Development, maintenance and disruption of the blood-brain barrier," *Nat. Med.*, vol. 19, no. 12, pp. 1584–1596, 2013.

[3] D. A. Nation *et al.*, "Blood–brain barrier breakdown is an early biomarker of human cognitive dysfunction," *Nat. Med.*, vol. 25, no. 2, pp. 270–276, 2019.

[4] S. Liebner *et al.*, “Structural alterations of tight junctions are associated with loss of polarity in stroke-prone spontaneously hypertensive rat blood–brain barrier endothelial cells,” *Brain Res.*, vol. 885, no. 2, pp. 251–261, 2002.
[5] D. D.C., “Blood-brain barrier breakdown in septic encephalopathy and brain tumours,” *J. Anat.*, vol. 200, no. 6, pp. 639–646, 2002.
[6] A. L. Bartels *et al.*, “Decreased blood-brain barrier P-glycoprotein function in the progression of Parkinson’s disease, PSP and MSA,” *J. Neural Transm.*, vol. 115, no. 7, pp. 1001–1009, 2008.
[7] Y. I. Wang, H. E. Abaci, and M. L. Shuler, “Microfluidic blood–brain barrier model provides in vivo-like barrier properties for drug permeability screening,” *Biotechnol. Bioeng.*, vol. 114, no. 1, pp. 184–194, 2017.
[8] B. Srinivasan, A. R. Kolli, M. B. Esch, H. E. Abaci, M. L. Shuler, and J. J. Hickman, “TEER Measurement Techniques for In Vitro Barrier Model Systems,” *J. Lab. Autom.*, vol. 20, no. 2, pp. 107–126, 2015.
[9] M. Odijk *et al.*, “Measuring direct current trans-epithelial electrical resistance in organ-on-a-chip microsystems,” *Lab Chip*, vol. 15, no. 3, pp. 745–752, 2015.
[10] O. Y. F. Henry, R. Villenave, M. J. Cronce, W. D. Leineweber, M. A. Benz, and D. E. Ingber, “Organs-on-chips with integrated electrodes for trans-epithelial electrical resistance (TEER) measurements of human epithelial barrier function,” *Lab Chip*, vol. 17, no. 13, pp. 2264–2271, 2017.
[11] J. Yeste, X. Illa, C. Gutiérrez, M. Solé, A. Guimerà, and R. Villa, “Geometric correction factor for transepithelial electrical resistance measurements in transwell and microfluidic cell cultures,” *J. Phys. D. Appl. Phys.*, vol. 49, no. 37, 2016.
[12] R. Booth and H. Kim, “Characterization of a microfluidic in vitro model of the blood-brain barrier (μBBB),” *Lab Chip*, vol. 12, no. 10, pp. 1784–1792, 2012.
[13] L. M. Griep *et al.*, “BBB on CHIP: Microfluidic platform to mechanically and biochemically modulate blood-brain barrier function,” *Biomed. Microdevices*, vol. 15, no. 1, pp. 145–150, 2013.
[14] J. A. Brown *et al.*, “Recreating blood-brain barrier physiology and structure on chip: A novel neurovascular microfluidic bioreactor,” *Biomicrofluidics*, vol. 9, no. 5, pp. 1–15, 2015.
[15] S. P. Deosarkar, B. Prabhakarpandian, B. Wang, J. B. Sheffield, B. Krynska, and M. F. Kiani, “A novel dynamic neonatal blood-brain barrier on a chip,” *PLoS One*, vol. 10, no. 11, pp. 1–21, 2015.
[16] F. R. Walter *et al.*, “A versatile lab-on-a-chip tool for modeling biological barriers,” *Sensors Actuators, B Chem.*, vol. 222, pp. 1209–1219, 2016.
[17] M. W. van der Helm *et al.*, “Direct quantification of transendothelial electrical resistance in organs-on-chips,” *Biosens. Bioelectron.*, vol. 85, pp. 924–929, 2016.
[18] J. A. Kim, H. N. Kim, S. K. Im, S. Chung, J. Y. Kang, and N. Choi, “Collagen-based brain microvasculature model in vitro using three-dimensional printed template,” *Biomicrofluidics*, vol. 9, no. 2, pp. 1–16, 2015.
[19] A. Herland, A. D. Van Der Meer, E. A. FitzGerald, T. E. Park, J. J. F. Sleeboom, and D. E. Ingber, “Distinct contributions of astrocytes and pericytes to neuroinflammation identified in a 3D human blood-brain barrier on a chip,” *PLoS One*, vol. 11, no. 3, pp. 1–21, 2016.
[20] N. J. Douville, Y. C. Tung, R. Li, J. D. Wang, M. E. H. El-Sayed, and S. Takayama, “Fabrication of two-layered channel system with embedded electrodes to measure resistance across epithelial and endothelial barriers,” *Anal. Chem.*, vol. 82, no. 6, pp. 2505–2511, 2010.
[21] N. J. Abbott, L. Rönnbäck, and E. Hansson, “Astrocyte-endothelial interactions at the blood-brain barrier,” *Nat. Rev. Neurosci.*, vol. 7, no. 1, pp. 41–53, 2006.
[22] M. W. Brightman, “Junctions Between Intimately Apposed Cell Membranes in the Vertebrate Brain,” *J. Cell Biol.*, vol. 40, no. 3, pp. 648–677, 2004.
[23] M. L. Schroeter *et al.*, “Astrocytes enhance radical defence in capillary endothelial cells constituting the blood-brain barrier,” *FEBS Lett.*, vol. 449, no. 2–3, pp. 241–244, 1999.
[24] M. W. van der Helm *et al.*, “Non-invasive sensing of transepithelial barrier function and tissue differentiation in organs-on-chips using impedance spectroscopy,” *Lab Chip*, vol. 19, no. 3, pp. 452–463, 2019.
[25] S. Grimnes and Ø. G. Martinsen, “Sources of error in tetrapolar impedance measurements on biomaterials and other ionic conductors,” *J. Phys. D. Appl. Phys.*, vol. 40, no. 1, pp. 9–14, 2007.
[26] D. B. Geselowitz, “An Application of Electrodynamic Lead Theory to Impendance Plethysmonography,” *IEEE Trans. Biomed. Eng.*, vol. 18, no. 1, pp. 38–41, 1971.
[27] S. Nag, A. Reichel, D. J. Begley, and N. J. Abbott, “An Overview of In Vitro Techniques for Blood-Brain Barrier Studies,” *Blood-Brain Barrier,* vol. 89, pp. 307–324, 2003.
[28] J. Wegener, S. Zink, P. Rösen, and H. J. Galla, “Use of electrochemical impedance measurements to monitor β-adrenergic stimulation of bovine aortic endothelial cells,” *Pflugers Arch. Eur. J. Physiol.*, vol. 437, no. 6, pp. 925–934, 1999.
[29] P. Somasundaran, *Encyclopedia of Surface and Colloid Science*, no. Volume 6. Taylor & Francis, 2006.
[30] H. S. Lee *et al.*, “Hydrogen peroxide-induced alterations of tight junction proteins in bovine brain microvascular endothelial cells,” *Microvasc. Res.*, vol. 68, no. 3, pp. 231–238, 2004.
[31] J. L. Lin, Y. H. Huang, Y. C. Shen, H. C. Huang, and P. H. Liu, “Ascorbic acid prevents blood-brain barrier disruption and sensory deficit caused by sustained compression of primary somatosensory cortex,” *J. Cereb. Blood Flow Metab.*, vol. 30, no. 6, pp. 1121–1136, 2010.
[32] D. E. Eigenmann, G. Xue, K. S. Kim, A. V Moses, M. Hamburger, and M. Oufir, “Comparative study of four immortalized human brain capillary endothelial cell lines, hCMEC/D3, hBMEC, TY10, and BB19, and optimization of culture,” *Fluids Barriers CNS*, vol. 10, p. 33, 2013.
[33] L. Cucullo *et al.*, “Immortalized human brain endothelial cells and flow-based vascular modeling: A marriage of convenience for rational neurovascular studies,” *J. Cereb. Blood Flow Metab.*, vol. 28, no. 2, pp. 312–328, 2008.
[34] J. H. Yeon, D. Na, K. Choi, S. W. Ryu, C. Choi, and J. K. Park, “Reliable permeability assay system in a microfluidic device mimicking cerebral vasculatures,” *Biomed. Microdevices*, vol. 14, no. 6, pp. 1141–1148, 2012.
[35] V. Siddharthan, Y. V Kim, S. Liu, and K. S. Kim, “Human astrocytes/astrocyte-conditioned medium and shear stress enhance the barrier properties of human brain microvascular endothelial cells,” *Brain Res.*, vol. 1147, no. 1, pp. 39–50, 2007.
[36] W. M. Pardridge, “Blood-Brain Barrier Drug Targeting: the Future of Brain Drug Development,” *Mol. Interv.*, vol. 3, no. 2, pp. 90–105, 2003.
[37] N. J. Abbott, A. A. K. Patabendige, D. E. M. Dolman, S. R. Yusof, and D. J. Begley, “Structure and function of the blood-brain barrier.,” *Neurobiol. Dis.*, vol. 37, no. 1, pp. 13–25, 2010.
[38] N. J. Abbott, “Role of intracellular calcium in regulation of brain endothelial permeability,” in *Introduction to the Blood–Brain Barrier*, 2009, pp. 345–353.
[39] M. A. Deli, “Potential use of tight junction modulators to reversibly open membranous barriers and improve drug delivery,” *Biochimica et Biophysica Acta - Biomembranes*, vol. 1788, no. 4. Elsevier B.V., pp. 892–

910, 2009.
[40] T. Sun, E. J. Swindle, J. E. Collins, J. A. Holloway, D. E. Davies, and H. Morgan, “On-chip epithelial barrier function assays using electrical impedance spectroscopy,” *Lab Chip*, vol. 10, no. 12, pp. 1611–1617, 2010.
[41] M. Nobles, P. A. Revest, P. -O Couraud, and N. J. Abbott, “Characteristics of nucleotide receptors that cause elevation of cytoplasmic calcium in immortalized rat brain endothelial cells (RBE4) and in primary cultures,” *Br. J. Pharmacol.*, vol. 115, no. 7, pp. 1245–1252, 1995.
[42] M. W. van der Helm, A. D. van der Meer, J. C. T. Eijkel, A. van den Berg, and L. I. Segerink, “Microfluidic organ-on-chip technology for blood-brain barrier research,” *Tissue Barriers*, vol. 4, no. 1. 2016.
[43] B. B. Weksler *et al.*, “Blood-brain barrier-specific properties of a human adult brain endothelial cell line,” *FASEB J.*, vol. 19, no. 13, pp. 1872–1874, 2005.

Supplementary Information

Assessing barrier properties using impedance spectroscopy in a semi-circular, blood-brain barrier on-chip

Fotios Avgidis

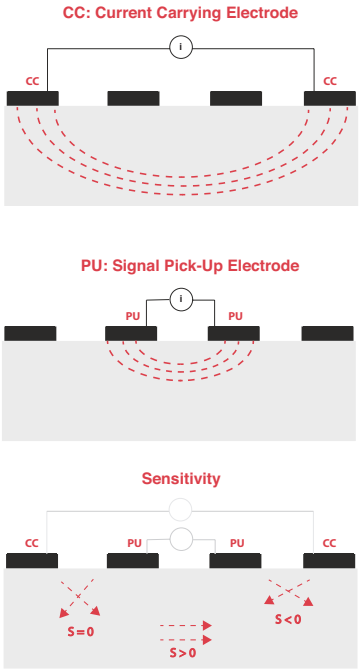

supplementary figure 1: sensitivity distribution illustration. Based on [1].

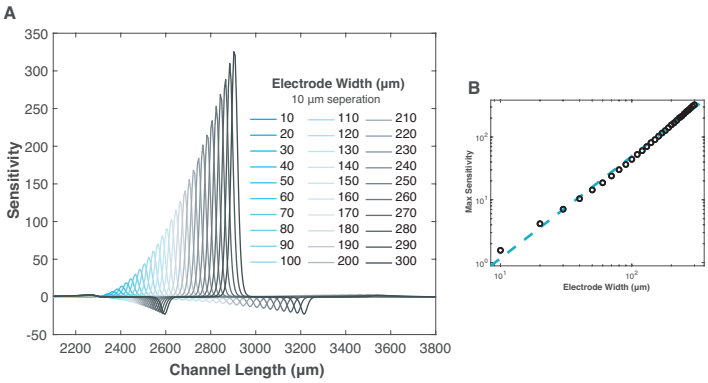

supplementary figure 2: scaling relationship between electrode width and sensitivity. The area between a single CC & PU electrode is shown. The sharp increase in sensitivity is always found in the region between the two electrodes. Fitted line: $y = x^{1.6} - 31$.

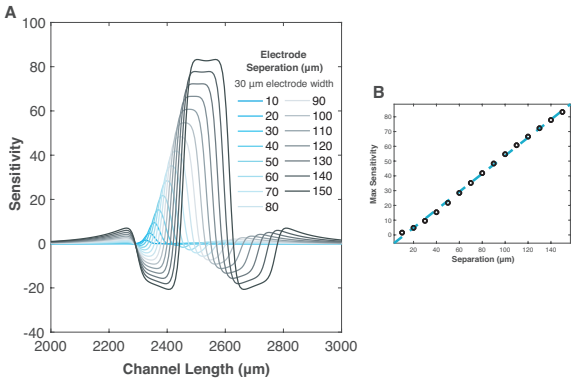

supplementary figure 3: scaling relationship between electrode separation and sensitivity. The area between a single CC & PU electrode is shown.

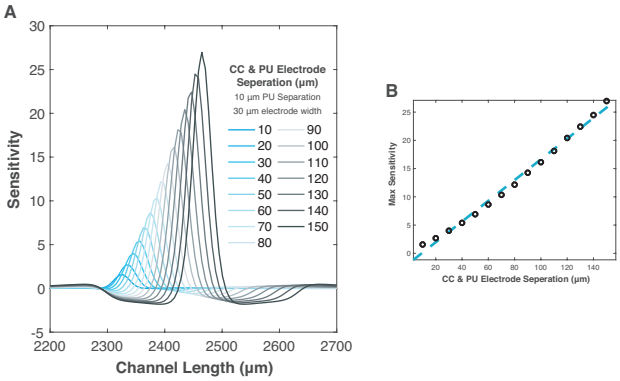

supplementary figure 4: scaling relationship between separation of CC & PU electrode sets and sensitivity. The area between a single CC & PU electrode is shown.

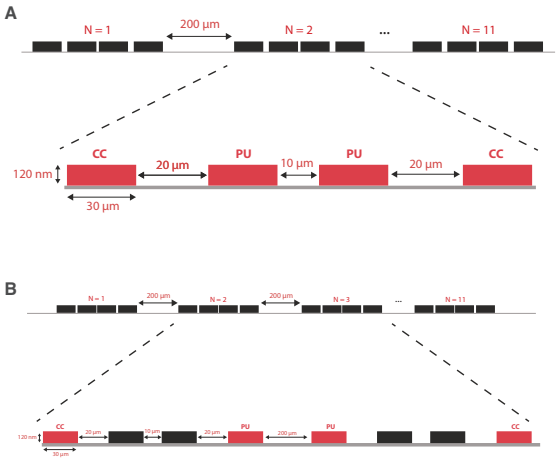

supplementary figure 5: final electrode design, 2D side view. (A) “regular’ topology (B) “interchanged” topology.

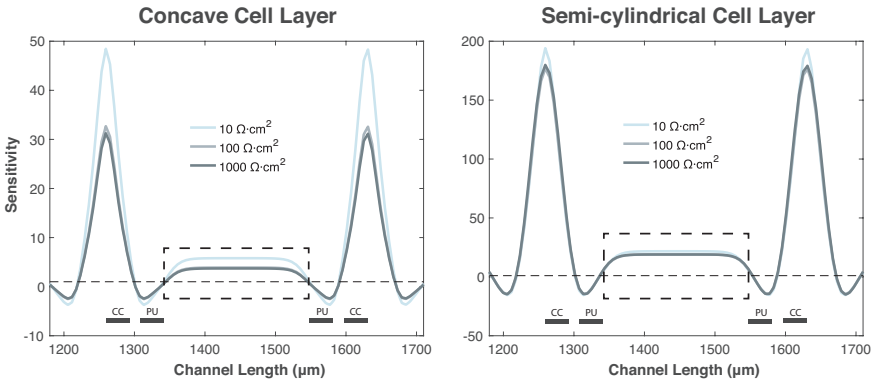

supplementary figure 6: electrode sensitivity of “regular” electrode configuration. The positions of electrodes are indicated on the bottom of the graph. The area within the dashed rectangular is used to extract the relationship between resistance and TEER (figure 2 of the main text).

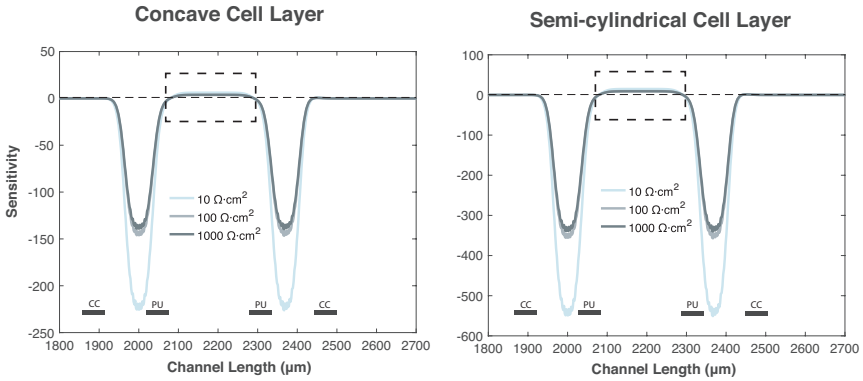

supplementary figure 7: sensitivity of “interchanged” electrode configuration. The positions of electrodes are indicated on the bottom of the graph. The area within the dashed rectangular is used to extract the relationship between resistance and TEER (figure 2 of the main text).

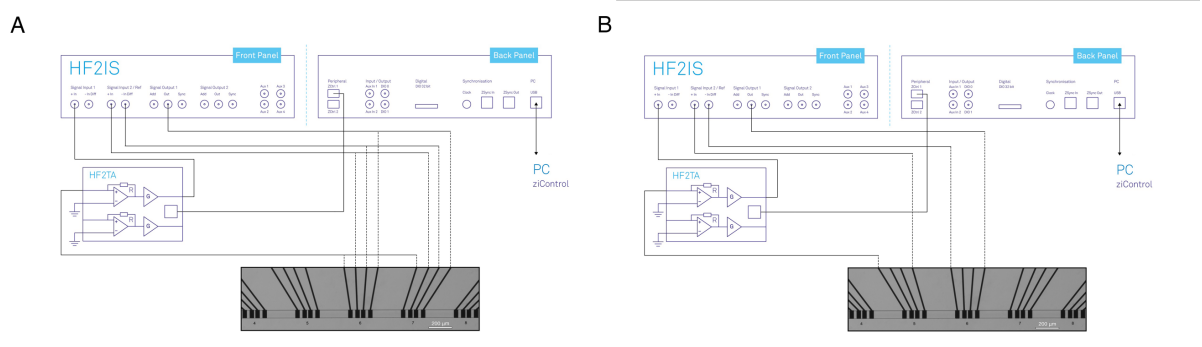

supplementary figure 8: connection topology of impedance spectroscope. (A) “regular’ topology (B) “interchanged” topology. Based on [2].

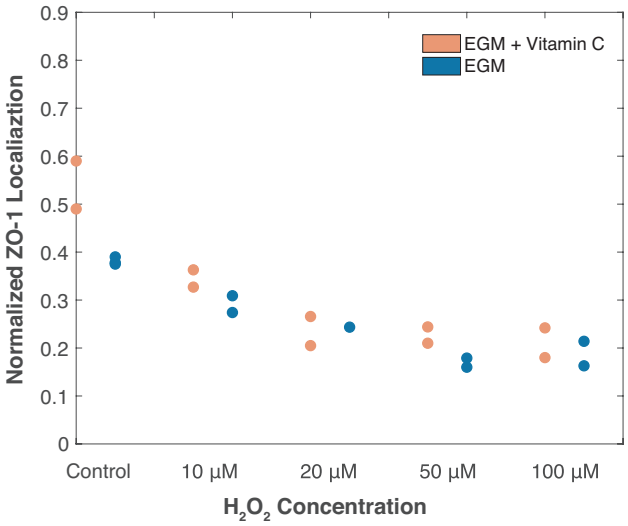

supplementary figure 9: Effect of vitamin C on tight junctions. Individual data points of figure 6.

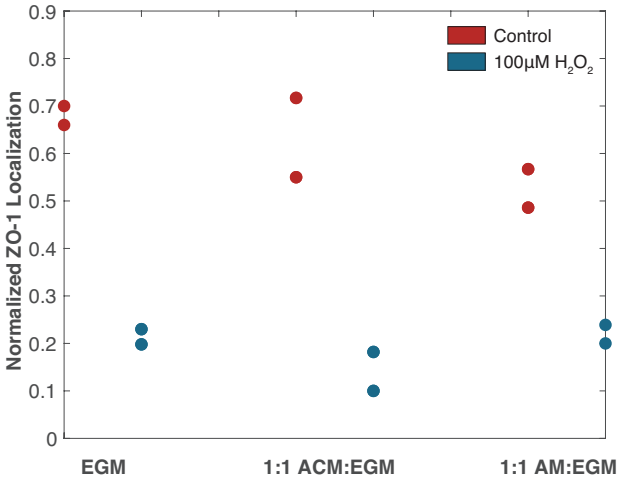

supplementary figure 10: Effect of ACM on tight junctions. Individual data points of figure 8.

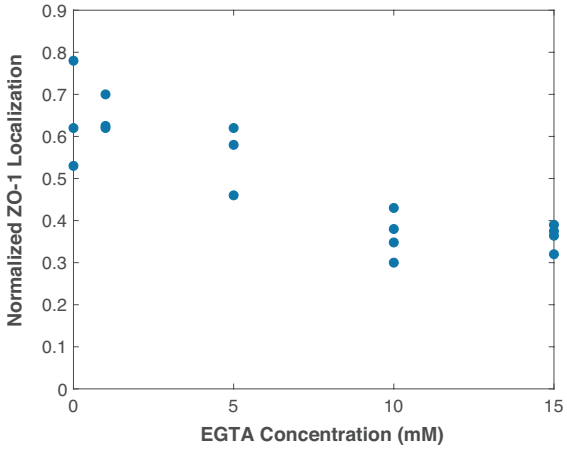

supplementary figure 11: Effect of EGTA on tight junctions. Individual data points of figure 11.

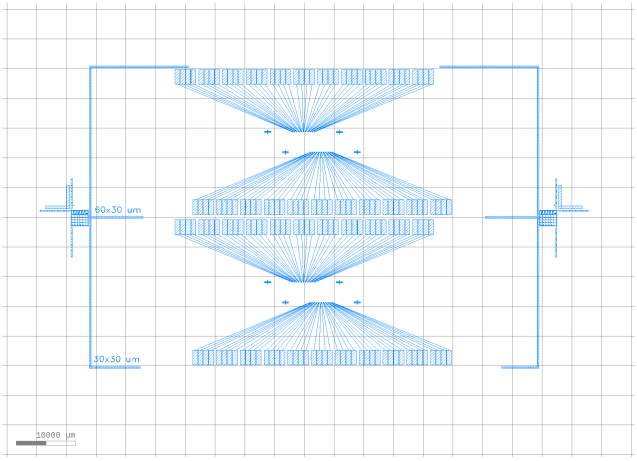

supplementary figure 12: mask design of electrode slide. Each wafer contains two sizes of electrodes: 60 x 30 µm and 30 x 30 µm. For the experiments presented in the main text we exclusively used the 60 x 30 µm electrodes.

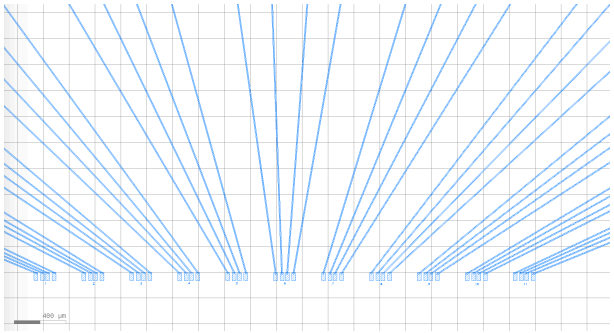

supplementary figure 13: magnified view of the 60 x 30 µm electrode mask design.

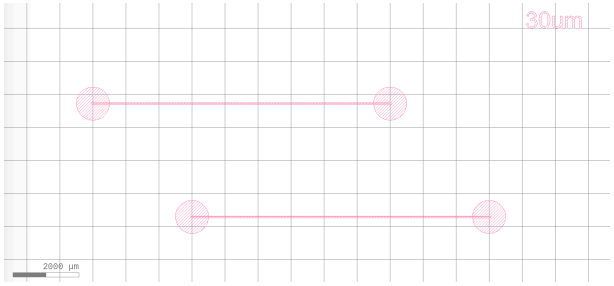

supplementary figure 14: mask design of the microfluidic channels. Each PDMS device contains two parallel channels.

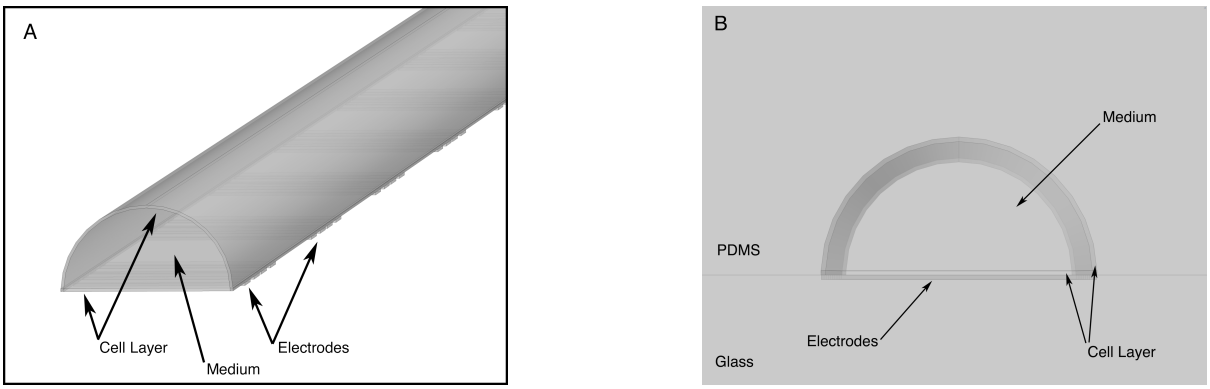

supplementary figure 15: geometric model used for the FEM study of the semi-circular cell layer. (A) Section of the channel (B) sideview of the channel.

Bibliography

[1] P. Kauppinen, J. Hyttinen, and J. Malmivuo, "Sensitivity Distribution Visualizations of Impedance Tomography Measurement Strategies," *Int. J. Bioelectromagn.*, vol. 8, no. 1, p. VII/1-VII/9, 2006.

[2] "HF2 User Manual." Zurich Instruments, p. 722.

Next page: Abstract submitted to MicroTAS 2019 conference

A 3D, MICROVASCULAR, BLOOD-BRAIN BARRIER ON CHIP

Fotios Avgidis[1], Martijn Tibbe[1], Anne Leferink[1], and Loes Segerink[1]
[1]BIOS - Lab on a Chip group, MESA+ Institute of Nanotechnology, Technical Medical Centre, and Max Planck Center for Complex Fluid Dynamics, University of Twente, THE NETHERLANDS

We have designed, fabricated, and characterized a microvascular, three-dimensional microfluidic model of the human blood-brain barrier with integrated electrodes that allow for real-time assessment of the barrier's integrity. The blood-brain barrier is a biological structure that acts as a "gatekeeper" between the central nervous system and the rest of the body. It controls the flux of solutes from the blood to the brain, only allowing chemicals that are necessary for neuronal functioning. Unlike previous efforts, our model reflects the actual size (diameter < 30 μm) and circular shape of a human brain microvessel [1], and achieves membrane-free separation of the basolateral and apical compartments [2-8].

We fabricated an array of microchannels in Polydimethylsiloxane (PDMS) which was then bonded on a glass substrate with embedded electrodes (fig.1). Thereafter, we coated the microchannels using fibronectin, an extracellular matrix protein, to allow cell attachment, and introduced human brain endothelial cells in the channels (HCMEC/d3, seeding density: 6 million cells/ml). After static incubation over a period of five days, the resulting microvasculature closely mimicked the size and shape of a human brain microvessel (fig.2).

To assess the barrier's electrical characteristics, we employed 4-terminal impedance spectroscopy using a combination of four out of the total 44 electrodes embedded under each microchannel. The presence of multiple electrodes allows us to independently address different micrometer-long regions of the microvessel. We developed an equivalent circuit model that reflects the electrical characteristics of the microvasculature and fit the experimental impedance data by means of a non-linear least-square fit with the transfer function of the circuit model in order to extract the cell layer resistance and capacitance (fig.3). Since the cell layer resistance is typically reported in the literature as TEER, we performed a numerical study using finite element analysis to create a model that translates cell layer resistance to TEER (fig.4). The electrode size and placement in the channel were optimized based on the numerical study to achieve high sensitivity and linearity between impedance and TEER.

Next, we used our engineered blood-brain barrier to elucidate the effect of vitamin C, a common antioxidant, against oxidative damage. We have grown microvasculatures in the presence and absence of vitamin C and then challenged them with hydrogen peroxide (H_20_2), a common oxidizer that damages tissue via oxidative stress [9]. The recorded impedance data revealed that a high dose of vitamin C results in a tighter cell monolayer (fig.5) but the relative change in impedance after H_20_2 incubation is similar in both cases. Since capacitance is a proxy for cell membrane surface area [10], we corrected for uneven cell layer coverage by normalizing the cell layer impedance with the capacitance. We verified this observation using tight-junction immunostaining on a two-dimensional culture (fig.6).

To summarize, we have developed a three-dimensional microfluidic blood-brain barrier model that accurately imitates human physiology *in vitro*, and allows for real-time electrical assessment of the barrier's properties. We subsequently employed this model to elucidate the role of antioxidants in oxidative stress.

Word Count: 491

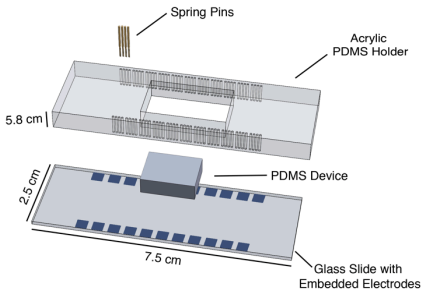

Figure 1: Overview of the Blood-brain barrier on chip device

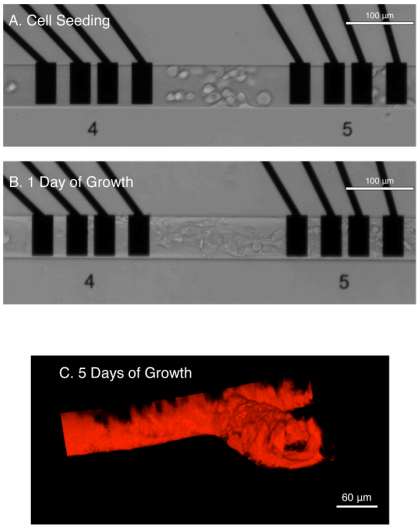

Figure 2: A. Micrograph of brain endothelial cells (hCMEC/D3) during seeding. B. Micrograph of the same cells after 24 hours of growth. C. Confocal image of cell layer after 120 hours of growth (red: F-actin).

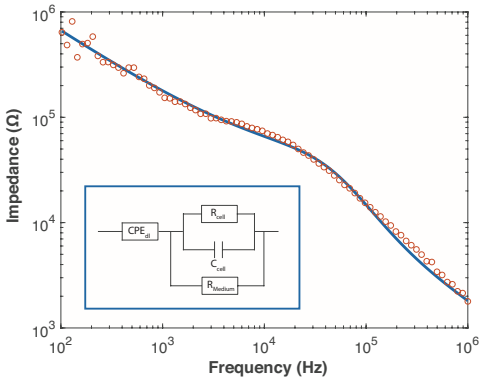

Figure 3. Typical impedance spectrum (symbols) and fit (solid line). Inset: Equivalent circuit used for the fit.

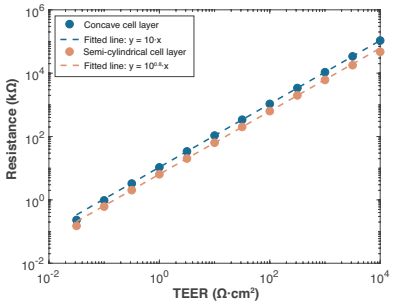

Figure 4: Scaling relationship between impedance and TEER.

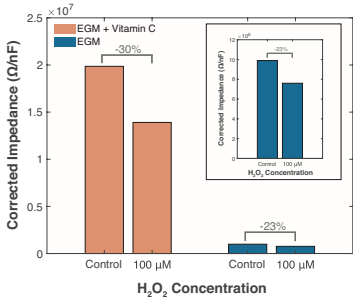

Figure 5. Impedance measurement in microvasculatures grown in the presence (1 mM) and absence of vitamin C. Inset: enlarged version of the impedance of cells grown in the absence of vitamin C.

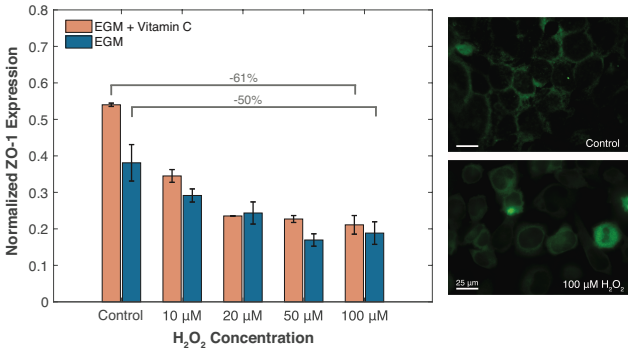

Figure 6. Control experiment (two-dimensional culture). Error bars are SEM (2 technical replicates per condition).

REFERENCES

[1] J. A. Kim et al., Biomicrofluidics, vol. 9, no. 2, pp. 1–16, 2015.
[2] R. Booth and H. Kim, Lab Chip, vol. 12, no. 10, pp. 1784–1792, 2012.
[3] L. M. Griep et al., Biomed. Microdevices, vol. 15, no. 1, pp. 145–150, 2013.
[4] J. A. Brown et al., Biomicrofluidics, vol. 9, no. 5, pp. 1–15, 2015.
[5] S. P. Deosarkar, et al., PLoS One, vol. 10, no. 11, pp. 1–21, 2015.
[6] F. R. Walter et al., Sensors Actuators, B Chem., vol. 222, pp. 1209–1219, 2016.
[7] M. W. van der Helm et al., Biosens. Bioelectron., vol. 85, pp. 924–929, 2016.
[8] Y. I. Wang, et al., Biotechnol. Bioeng., vol. 114, no. 1, pp. 184–194, 2017.
[9] J. H. Yeon, et al., Biomed. Microdevices, vol. 14, no. 6, pp. 1141–1148, 2012.
[10] O. Y. F. Henry, et al., Lab Chip, vol. 17, no. 13, pp. 2264–2271, 2017.